

AperTO - Archivio Istituzionale Open Access dell'Università di Torino

Synthesis, characterization and CO₂ uptake of a chiral Co(II) Metal-Organic Framework containing a thiazolidine-based spacer

This is the author's manuscript

Original Citation:

Availability:

This version is available <http://hdl.handle.net/2318/102573> since 2016-10-08T15:18:05Z

Published version:

DOI:10.1039/C2JM16236A

Terms of use:

Open Access

Anyone can freely access the full text of works made available as "Open Access". Works made available under a Creative Commons license can be used according to the terms and conditions of said license. Use of all other works requires consent of the right holder (author or publisher) if not exempted from copyright protection by the applicable law.

(Article begins on next page)



UNIVERSITÀ DEGLI STUDI DI TORINO

This is an author version of the contribution published on:

Questa è la versione dell'autore dell'opera:

Synthesis, characterization and CO₂ uptake of a chiral Co(II) Metal-Organic Framework containing a thiazolidine-based spacer

Andrea Rossin, Barbara Di Credico, Giuliano Giambastiani, Maurizio Peruzzini, Gennaro Pescitelli, Gianna Reginato, Elisa Borfecchia, Diego Gianolio, Carlo Lamberti, Silvia Bordiga

J. Mater. Chem., **2012**, 22, 10335–10344

DOI: 10.1039/c2jm16236a

The definitive version is available at:

La versione definitiva è disponibile alla URL:

<http://pubs.rsc.org/en/Content/ArticleLanding/2012/JM/C2JM16236A>

Synthesis, characterization and CO₂ uptake of a chiral Co(II) Metal-Organic Framework containing a thiazolidine-based spacer†

Andrea Rossin,^{*a} Barbara Di Credico,^a Giuliano Giambastiani,^a Maurizio Peruzzini,^{*a} Gennaro Pescitelli,^b Gianna Reginato,^a Elisa Borfecchia,^c Diego Gianolio,^c Carlo Lamberti,^c Silvia Bordiga^c

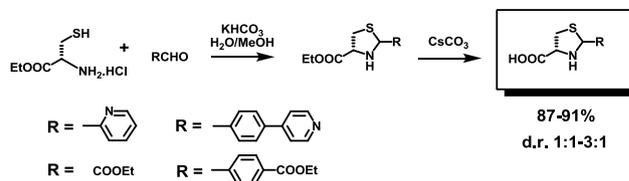
5 The polytopic ligand thiazolidine-2,4-dicarboxylic acid (**H₂L**) has been synthesised on a large scale starting from the naturally occurring amino acid L-cysteine. The (*R,R*)/(*S,R*) diastereomeric mixture has been separated into its constituents through selective precipitation of the pure (*R,R*) isomer from concentrated H₂O/MeOH solutions. The enantiomerically pure ligand (**H₂L-RR**) has been reacted with 10 CoCl₂ · 6H₂O under hydrothermal conditions, the final product being [Co(**L-RR**)(H₂O) · H₂O]_∞ (**1**). The obtained coordination polymer is optically pure, and it maintains the chiral information that is present in its building block. Two different kind of channels are present in the 3D structure of **1**: one hydrophobic (with the sulfur atoms of the thiazolidine rings exposed) and the other hydrophilic [with the *aquo* ligand on Co(II) exposed, and hosting the crystallization water solvent]. **1** has been characterized through a 15 combination of X-ray diffraction (single-crystal and powder) and spectroscopic (CD, IR, UV-Vis, XANES, EXAFS) techniques. Finally, CO₂ adsorption tests conducted at 273 K and (pCO₂)_{max} = 920 torr have shown a good carbon dioxide uptake, equal to 4.7 wt.%.

1. Introduction

20 During the last twenty years, metal-organic frameworks (MOFs) chemistry has witnessed an extraordinary boost, mostly because of the virtually infinite number of combinations between organic linkers and inorganic Secondary Building Units conceivable.¹ A rapidly growing area of investigation is that related to chiral MOFs.² There are a number of literature cases 25 where chiral frameworks are generated by *achiral* flexible ligands like dihydroxymalonate (mesoxalate),³ pyridine-4,5-imidazoledicarboxylic acid,⁴ 3,5-pyridine dicarboxylate.⁵ The chirality is generated by the way the ligands bind to the metal ions with a *helicoidal* crystal packing in the solid state (the MOF 30 crystallographic space group will also be chiral). A stereogenic center is created upon complexation of the metal ions, and if all of them keep the same Λ- or Δ- configuration the crystal will be chiral, the reaction yielding equivalent quantities of both MOF crystal enantiomorphs (*spontaneous resolution* upon 35 crystallization). Nonetheless, the main synthetic strategy to obtain chiral crystals is based upon the use of optically pure multidentate ligands as MOFs constituents, with literature examples spanning from readily available natural products from the chiral pool like amino acids (asparagine,⁶ tyrosine,⁷ histidine,⁸ glutamic acid⁹), 40 tartaric acid¹⁰ and saccharic acid¹¹ to tailor-made rigid *spiro* bicyclic compounds,¹² axial chiral binaphthyl linkers² or salen-based ligands containing (*R,R*)-cyclohexanediamine as organic skeleton.¹³ In the latter group, the main synthetic effort required is associated to achieve an enantiomerically enriched linker. 45 From this point of view, the most useful approach is that of designing a stereoselective synthesis of the desired spacer. Among the plethora of advanced asymmetric synthetic methodologies currently available, the synthetic elaboration of a cheap and enantiopure precursor derived from the chiral pool is 50 attractive and often successfully used. The stereochemical information present in the chiral organic building block obtained in this way can be maintained into the final polymer, thus

generating chiral MOFs with several important applications in the fields of enantioselective separation, chiral sensing, non linear 55 optics¹⁴ and enantioselective heterogeneous catalysis.^{2,15}

Our group has recently turned the attention to the development of synthetic protocols for multi-gram syntheses of thiazolidine-containing polytopic carboxylates via the synthetic elaboration of the naturally occurring amino acid L-cysteine (Scheme 1).¹⁶



Scheme 1. Syntheses of thiazolidine-containing polytopic ligands.

Hereafter, we report on the synthesis and characterization of a 65 Co(II) coordination polymer containing the enantiomerically pure ligand (*R,R*)-thiazolidine-2,4-dicarboxylic acid (**H₂L-RR**, see Scheme S1): [Co(**L-RR**)(H₂O) · H₂O]_∞ (**1**). The material has been characterized through crystallographic (single crystal and powder XRD) and spectroscopic (IR, UV-Vis, XANES and EXAFS) 70 techniques. As already proven for the characterization of several different coordination polymers, the synergic use of crystallographic and spectroscopic approaches leads to a comprehensive understanding of the structural, vibrational and electronic properties of such complex materials.¹⁷ In the present 75 case, owing to the chiral nature of the investigated MOF, solid-state Circular Dichroism (CD) has also been exploited for its characterization.¹⁸ The technique, developed especially for inorganic complexes,¹⁹ measures the CD signal of a microcrystalline sample in a mixture with an inert salt (KCl or 80 KBr), and it is useful to complement X-ray diffraction analyses of

crystals.²⁰

2. Results and discussion

2.1. Synthesis and X-ray crystal structure.

5 Hydrothermal conditions in Teflon-lined stainless steel autoclaves were employed to react the (*R,R*) diacid (**H₂L-RR**) with Cobalt(II) chloride hexahydrate, to afford single crystals of **1** as the sole product after heating at 90 °C for 24h. The crystal structure of **1** (Figure 1a) revealed that the ligand is tridentate on
10 Co(II) through two oxygen atoms from each of the carboxylate arms {d[Co-O(2)] = 2.056(2) Å; d[Co-O(3)] = 2.080(2) Å} and the nitrogen atom of the ring {d[Co-N(1)] = 2.154(3) Å}. The other oxygens from the carboxylate groups act as bridge between adjacent metal centres {d[Co-O(1)] = 2.069(2) Å; d[Co-O(5)] =
15 2.109(2) Å}, thus forming the 3D polymeric lattice. The ligand coordination mode to Co(II) is similar to that found in the corresponding unsaturated thiazoles.²¹ The octahedral metal coordination geometry is completed by an aquo ligand *trans* to O(2) {d[Co-O(4)] = 2.075(3) Å}, that engages in extensive
20 hydrogen bonding with the neighbouring oxygen atoms in the cell (see Table S5). The compound has a tetragonal lattice, and crystallizes in the chiral *P4₁* space group. The presence of the screw axis along the *c* direction generates symmetrical channels of two different types: one hydrophobic, where the S atoms of the
25 thiazolidine rings are exposed, and the other hydrophilic, containing the aquo ligands and the other crystallization water molecules (Figure 1b). This intriguing feature could be exploited for selective host-guest interaction with molecules of opposite polarity.^{11,22}

30

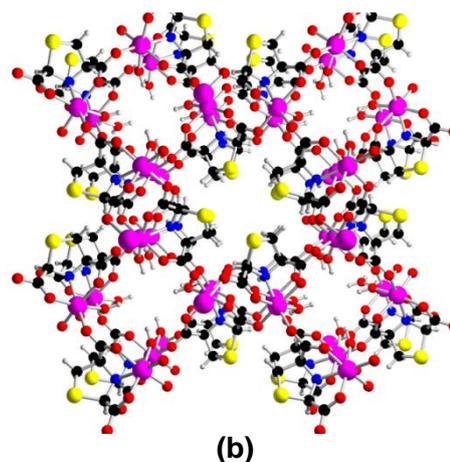
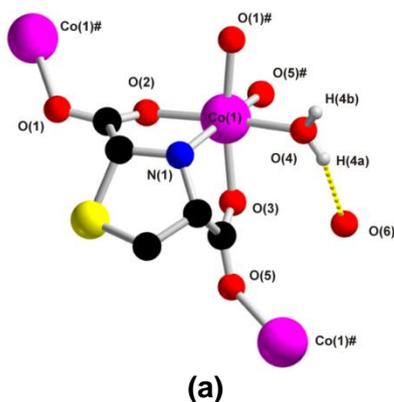


Figure 1. Part (a): Cobalt(II) coordination sphere in **1** (H atoms on the ligand omitted for clarity, Co-OH₂...OH₂ hydrogen bond between the coordinated and crystallization water molecules in yellow dotted line).
35 Part (b): 3D polymeric lattice of **1** (viewed along the *c* axis, crystallization water molecules omitted for clarity). Atom color code: magenta, Co; black, C; white, H; blue, N; yellow, S; red, O.

Powder X-ray diffraction run on the batch confirmed the phase
40 purity, from comparison of the experimental diffractogram with the simulation coming from the single-crystal solution (see Figure S2). The final product does not depend on the counterion: the reaction carried out either with cobalt(II) nitrate hydrate [Co(NO₃)₂ • 6H₂O] or acetate hydrate [Co(OAc)₂ • 4H₂O] under
45 the same experimental conditions always led to **1**, with comparable yield. Furthermore, the reaction also seems to be solvent-independent: **1** is again the reaction outcome when replacing water with methanol or DMF in the solvothermal process; however, microcrystalline powders instead of single
50 crystals were obtained in the latter cases. As for the metal ion, when using zinc(II) perchlorate hydrate [Zn(ClO₄)₂ • 6H₂O] as starting material, colorless crystals of the isostructural compound [Zn(L-RR)(H₂O) • H₂O]_∞ (**2**) were isolated.²³ Unfortunately, the analysis of the powder X-ray diffractogram of the solid batch
55 revealed that this phase is not pure: from a comparison with the data present within the diffractometer database, the impurity can be identified with zinc(II) chlorite dihydrate [Zn(ClO₂)₂ • 2H₂O].²⁴ The latter is a possible by-product of a redox reaction occurring between the (oxidizing) perchlorate ion and the sulfide
60 group on the thiazolidine ring (with concomitant formation of the corresponding sulfoxide, see Scheme S2). The employ of salts containing non-oxidizing counterions, like chloride (ZnCl₂), fluoride (ZnF₂) or acetate [Zn(OAc)₂ • 2H₂O] either provided no polymeric crystalline products or led to decomposition. Thus, **2**
65 was not taken into account for further investigation. Remarkably, attempts made with the other ligand diastereoisomer [the *trans* (*S,R*) form, see Scheme S1] did not lead to any coordination polymer or metal complex, under the same experimental conditions. Apparently, the *cis* carboxylate orientation is essential
70 to build a 3D polymeric structure.

2.2. Thermal stability.

The thermal behaviour of **1** was assessed through TGA-MS and

variable temperature PXRD analyses, see Figures S3 and S4, respectively. The TGA profile reveals that both crystallization and coordination water is almost completely lost in the 30-220 °C range (12.4 wt% loss vs. 13.2 wt% theoretically calculated). According to the PXRD measurements, the anhydrous polymeric framework is thermally stable and retains its crystalline texture up to 220 °C; the coordinated water loss is confirmed by the disappearance of the main peak at $2\theta = 6^\circ$ (corresponding to a d -spacing of 12.35 Å) together with other minor peaks in the $21^\circ \leq 2\theta \leq 24^\circ$ interval, as judged from the comparison with the simulated pattern of the anhydrous $[\text{Co}(\text{L-RR})_\infty]$ phase ($\mathbf{1}_{\text{act}}$) built from the single crystal data (Figure S5). Above 280 °C ($T_{\text{onset}} = 286^\circ\text{C}$ – see Figure S3), the framework collapses with concomitant loss of the long-range order and formation of an amorphous domain.

The retention of the 3D scaffold after water loss may be important in view of the generation of chemically active exposed metal sites, as evidenced in other literature examples.²⁵ In the case of Co(II), the only existing case (to the best of our knowledge) is that published by Zhou *et al.* in 2006 with a triazine-based linker,²⁶ where the square pyramidal metal coordination geometry reminds that of Vitamin B₁₂. Shape- and size-selective guest diffusion into the MOF channels can lead to chemical activation by the coordinatively unsaturated Co(II) ions. The modification of the metal coordination sphere is better evidenced by the XANES/EXAFS and UV-Vis spectroscopies, see Sections 2.4 and 2.6.

2.3. Circular dichroism.

The microcrystalline solid state CD spectrum of **1** (KCl pellet, see Figure 2) proves that the compound is indeed optically active and not a racemate. It shows bands in two distinct regions, including a very broad and structured positive band between 460-610 nm and two narrower bands at high energy, a first and more intense negative one at 255 nm, and a second weak positive one with maximum at 230 nm. The low-energy CD band is due to metal-centered $d-d$ transitions. The anisotropy or g -factor for this band amounts to $g = \Delta A/A = +2 \cdot 10^{-3}$, the order of magnitude expected for metal $d-d$ transitions which are allied with large magnetic transition and small electric transition moments.²⁷ Natural (not magnetic) CD spectra of octahedral Co(II) complexes have been scarcely considered,²⁸ especially in comparison with the extensive work done on Co(III) and tetrahedral Co(II) complexes.²⁹ The position and shape of the $d-d$ CD band recall the main absorption band observed for symmetrical (O_h or D_{3d}) octahedral Co(II) complexes in the 450-625 nm region,²⁹ which is due to the ${}^4T_{1g}(P) \leftarrow {}^4T_{1g}(F)$ transition of the high-spin d^7 system. In the case of compound **1**, obviously, any degeneracy in d state levels is removed due to the lack of symmetry elements in the coordination core. The short wavelength region is of more difficult interpretation. In fact, the differences observed between the CD spectrum of **1** and that of the free ligand **H₂L-RR** (see Figure S1) may be due to various and possibly concomitant reasons: a) a change in the ligand conformation upon complexation; b) the coupling between electronic transitions belonging to different ligands put close together in the crystal lattice; c) the contribution from other

metal-centered or ligand/metal charge transfer transitions.

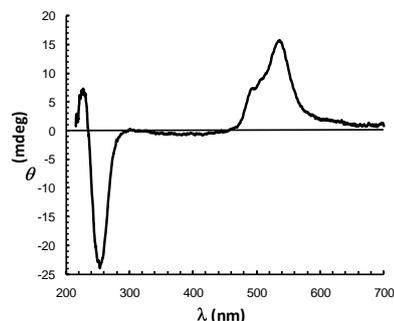


Figure 2. Solid-state CD spectrum of **1** measured on a KCl pellet obtained as discussed in the Experimental Section. The spectrum is not normalized and shown in ellipticity θ units (millidegrees).

2.4. X-ray absorption spectroscopy.

2.4.1. XANES study. K-edge XANES provides information on the unoccupied states reachable by promotion of a $1s$ electrons and is consequently dependent on the local coordination and symmetry around the absorbing atom. Figure 3a shows the effect of the activation on the Co K-edge spectra of **1**. The main changes can be summarized as follows: (i) a decrease of the white line intensity (first resonance after the edge, from 1.59 to 1.48) without any apparent shift; (ii) the appearance of a new electronic transition around 7716 eV (more evident after the if compared with that of the CPO-27-Ni MOF,³⁰ Figure 3b); (iii) the intensity increase (from 0.039 to 0.059) and a small red shift (from 7709.7 eV to 7709.3 eV) of the very weak pre-edge feature (see inset in Figure 3a), due to a dipole forbidden $1s \rightarrow 3d$ electronic transition. The significant reduction of the white line intensity reflects the decrease of the average coordination of the absorbing atom.³¹ No $1s \rightarrow 4p$ distinct (Figure 3a) electronic transitions are observed for the hydrated sample, probably because too close to the edge to be resolved. Water removal causes a symmetry change for Co(II) from octahedral-like to square-pyramidal-like implying the removal of the degeneration of p -levels (splitting between p_z and p_x, p_y , being xy the pyramidal plane) and the loss of the inversion center. Consequently, a new pre-edge component appears upon dehydration at 7716 eV, which is attributed to the $1s \rightarrow 4p_z$ electronic transition. The splitting of the $1s$ to $4p$ level transitions has already been observed in the XANES spectra for other metal centers when the p degeneration was removed by symmetry reduction.³² Finally, the very weak pre-edge feature around 8333 eV increases in intensity upon dehydration, because of the loss of the inversion center. This symmetry change also accounts for the increase of the component due to the $1s \rightarrow 3d$ electronic transition, that is forbidden for a perfect O_h symmetry.

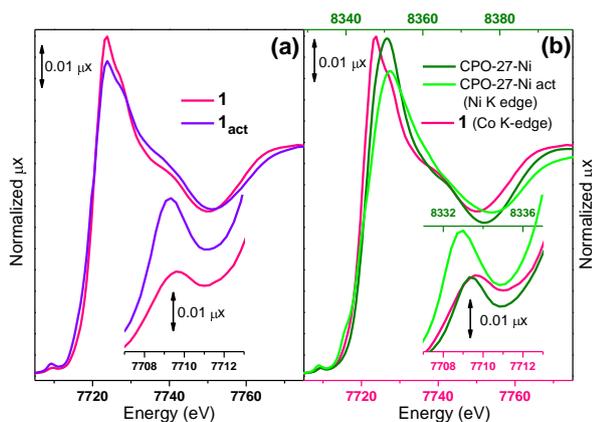


Figure 3. Part (a): Co K-edge XANES spectra, normalized to the edge jump, of **1** (pink) and **1_{act}** (violet). The inset reports a magnification of the dipole forbidden, $1s \rightarrow 3d$ electronic transition. Part (b) top abscissa axes: as part (a) for the Ni K-edge XANES spectra of CPO-27-Ni MOF before
 5 (dark green) and after (light green) activation.³⁰ The Co K-edge XANES spectrum of **1** (pink) is also reported (bottom abscissa axes). To allow a direct comparison, in both main part and inset, the same intervals have been reported, just shifted by 624 eV,³³ that is the difference between Co (7709 eV) and Ni (8333 eV) K-edges in metal compounds: 7707-7775 eV
 10 and 7707-7713 eV (inset) for the Co K-edge and 8329-8399 eV and 8331-8337 eV (inset) for the Ni K-edge.

The analogy between the evolution of the Co K-edge XANES spectra of **1** upon activation (Figure 3a) and the corresponding
 15 ones obtained at the Ni K-edge on CPO-27-Ni MOF (Figure 3b, top ordinate axes) is striking. CPO-27-Ni is a Ni(II) MOF, where the metal ion exhibits an O_h -like symmetry, being surrounded by five framework oxygen atoms and one coordinated water molecule in its first coordination shell, the latter being lost upon
 20 activation.³⁰ The same points discussed above for the activation of **1** are observed in the evolution from the dark green to the light green curve in Figure 3b, and they can be commented in exactly the same way. Interestingly, when the XANES spectrum of **1** (Figure 3b, pink curve, bottom ordinate axes) is superimposed to
 25 that of CPO-27 Ni (Figure 3b, dark green curve, top ordinate axes) the two spectra look extremely similar (with the pre-edge peaks perfectly aligned); the white lines and post edge features are at the same relative energy from the pre-edge peak within 2 eV. The presence of a nitrogen atom in the first coordination shell
 30 of **1** does not modify its XANES spectrum dramatically with respect to that of CPO-27-Ni (with only O atoms in the first shell). This is due to the low Z contrast between O and N atoms, that are almost indistinguishable in X-ray absorption spectroscopies, while they could be separated in X-ray emission
 35 spectroscopy.³⁴

2.4.2. EXAFS study. The experimental EXAFS spectra of **1** (pink) and **1_{act}** (violet) are reported in Figure 4, in both k - and R -spaces. Moving from **1** to **1_{act}**, a shift towards shorter R -values and a
 40 decrease of the amplitude related to the first shell signal was observed. Both effects are a consequence of the overall bond lengths contraction after the *aquo* ligand loss during the thermal activation, and the consequent formation of a coordination vacancy on Co(II). A similar effect was observed in the activation

45 for the local environment of Cu(II) in HKUST-1³⁵ or Ni(II) in CPO-27-Ni.³⁰

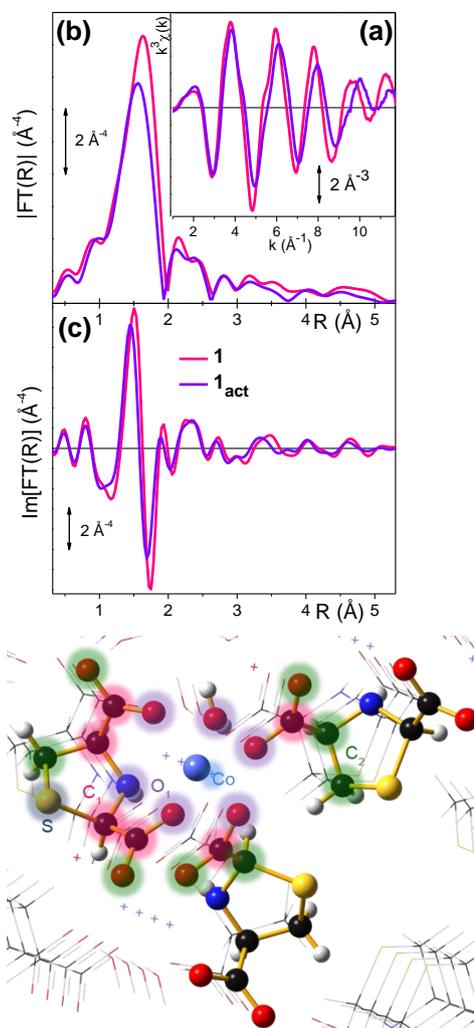


Figure 4. Part (a): Comparison between experimental k^3 -weighted EXAFS data for **1** (pink) and **1_{act}** (violet). Part (b): modulus of the phase
 50 uncorrected FT of the EXAFS spectra reported in part (a). Part (c): as part (b) for the imaginary part of the FT. Part (d): the cluster (built from the XRD structure) used to compute phases and amplitudes of all paths used
 55 in the fit of the EXAFS spectrum of **1**. Atoms color code is the following: Co pink, C black, O red, H white, N blue, S yellow. The three different shells of low-Z atoms and the high-Z Co and S atoms contributing to EXAFS signal are highlighted by different colored halos. See Figure S8 of the ESI for a larger view of the cluster embedded in the MOF framework.

60 For **1**, the structure used as starting point for the fitting procedure is shown in Figure 4d, where the three different shells are highlighted by differently colored halos. The first shell (atoms with violet halo) includes four oxygens plus one nitrogen atoms from the ligand and the oxygen of the water molecule; the second
 65 shell (atoms with pink halo) contains 1 O and 6 C atoms at a distance of about 3 Å from the Co atom; the third shell (atoms with green halo) includes C, O and N atoms at distances higher than 3.7 Å (see first column of Table 1). Not all the atoms

Table 1. Summary of the parameters optimized in the fitting of the EXAFS data on the pristine and activated sample (see Figure 5). The fits were performed in R-space in the $\Delta R = 1.00\text{--}5.20 \text{ \AA}$ range over k^3 -weighted FT of the $\chi(k)$ functions performed in the $2.0\text{--}11.8 \text{ \AA}^{-1}$ interval. A single ΔE_0 and a single S_0^2 have been optimized for all SS and MS paths.

Selection of atomic distances from Co(1) atom from the single crystal XRD study	Summary of the EXAFS data analysis		
Sample 1	Parameter	Sample 1	Sample 1_{act}
	Independent points	26	26
	Optimized variables	12	12
	R-factor	0.007	0.037
	S_0^2	0.96 ± 0.04	1.0 ± 0.1
	ΔE (eV)	2.0 ± 0.5	1 ± 1
First coordination shell (low Z elements)			
Co(1)-O(2) = 2.056; Co(1)-(O3) = 2.069; Co(1)-O(O3) = 2.074; Co(1)-(O1#) = 2.080; Co(1)-O(O5#) = 2.109; Co(1)-(N1) = 2.155	ΔR_1 (\AA)	0.000 ± 0.004	-0.050 ± 0.008
	σ_1^2 (\AA^2)	0.007 ± 0.001	0.008 ± 0.001
Second coordination shell (low Z elements)			
Co(1)-C = 2.841; 2.876; 2.945; 2.978; 2.985; 3.118; Co(1)-O = 3.289	ΔR_2 (\AA)	0.08 ± 0.03	0.02 ± 0.04
	σ_2^2 (\AA^2)	0.011 ± 0.002	0.009 ± 0.006
Successive coordination shells (low Z elements)			
Co(1)-C, Co(1)-O and Co(1)-N distances in the 3.739- 5.150 range	ΔR_3 (\AA)	0.1 ± 0.1	0.0 ± 0.2
	σ_3^2 (\AA^2)	0.02 ± 0.01	0.02 ± 0.03
Higher Z scattering contributions			
Co(1)-S(1) = 4.257; 5.205	ΔR_S (\AA)	-0.02 ± 0.06	-0.2 ± 0.1
	σ_S^2 (\AA^2)	0.011 ± 0.008	0.01 ± 0.02
Co(1)-Co(1#) = 5.150; 5.265	ΔR_{Co} (\AA)	-0.05 ± 0.03	-0.10 ± 0.09
	σ_{Co}^2 (\AA^2)	0.011 ± 0.004	0.01 ± 0.01

belonging to the last group are highlighted in Figure 4d, since they are not part of ligand molecules directly bound to the Co absorber. The detailed description of the adopted fitting procedure is reported in the SI. Given the similar electronic number for C, O, and N ($\Delta Z = 2$ or 1), their scattering amplitude (and the related contribution to the overall EXAFS scattering) will be very similar. Thus, these atoms were treated in the same way, optimizing from all of them the same displacement from the atomic coordinates (ΔR_i , $i = 1, 2$ or 3) and the same Debye-Waller factor (σ_i^2 , $i = 1, 2$ or 3). On the other hand, a different approach was required for the higher-Z atoms such as S and Co (different from the absorber), which needed a special set of ΔR and σ^2 parameters. Including an energy shift ΔE and an amplitude factor, shared among all SS and MS paths, the complete fitting model needed 12 independent parameters. As for the MS paths, the ΔR were calculated according to geometrical constraints starting from the ΔR of the involved atoms, while the Debye-Waller factors were summed according to the following rule: $\sigma_{MS}^2 = \sigma_1^2 + \sigma_2^2$, where σ_1, σ_2 corresponds to the Debye-Waller factors of the atoms involved in the MS. For **1_{act}**, a similar procedure was applied, after removal of the water molecule from the Co(II) coordination sphere of **1** to get the initial guess structure for the data refinement. The fits for both **1** and **1_{act}**

samples are reported in Figure 5. In both cases, the theoretical curves reproduce very well the experimental EXAFS spectra. The R-factor values are below 1 and 4% for the fits of **1** and **1_{act}**, respectively. The impressive quality of the fit obtained for **1** is a direct strong validation of the validity of the single crystal XRD refinement, used as input in the EXAFS data analysis. Such single crystal XRD data were not available for **1_{act}**. The satisfactory EXAFS data fitting for **1_{act}** implies that the local environment around Co(II) is only partially perturbed by the dehydration; if so, a model created from the as-synthesized structure can indeed reproduce very well the experimental EXAFS spectrum of the activated phase. The quality of both fits can be further confirmed by the low correlations among the fitted parameters: $S_0^2/\sigma_1^2 = 0.88$ and $\Delta E/\Delta R_1 = 0.82$ for **1** and $S_0^2/\sigma_1^2 = 0.84$ and $\Delta E/\Delta R_1 = 0.81$ for **1_{act}**, respectively. In the bottom panels of Figure 5 (left panel and right panels for sample **1** and **1_{act}**, respectively) the different paths contributions to the imaginary part of the FT were reported. The most intense signal is mainly coming from SS paths involving first shell atoms. We tried to distinguish between the signal coming from the ligand N atom or the water molecule O (in the as-synthesized sample) atom and that due to the remaining four O atoms of the TIDA ligands. Even using different parameters, we obtained the same

results in the fit, concluding that the discrimination is impossible because of the very similar Z and distances from the absorber. The low- R region, indicatively up to 2.5 Å, is well reproduced adding to the first shell also the SS paths related to the second shell atoms. In the region 2.5-4 Å different SS and MS paths contributes to the overall signal. In the high- R region (distances longer than 4 Å), the dominant contribution is assigned to Co-Co SS. Looking at the optimized parameters resulting from the fits, we obtained for both samples comparable energy shifts and S_0^2 parameters equal to 1 within the experimental error. The Debye-Waller factors assume values comparable within the errors in the two fits for all the different shells of atoms; generally, the values are proportional to the distance from the absorber and to the number of electrons of the scattering atom. The ΔR values reported in the last column of Table 1 represent the difference between distances optimized in the single crystal XRD and EXAFS refinement of **1**. With the only exception of the C atoms contributing to the second shell environment, in all the other cases XRD and EXAFS refinement agree within the EXAFS experimental error (those of XRD where neglected here, as significantly smaller). The overestimation of the second shell distances by EXAFS is probably due by a systematic error induced by the strong contribution that MS paths have in the same R -region, see Figure 5. The Co-Co path length also shows a slight shortening. In this case, the EXAFS result is more reliable as the scattering of Co atoms dominates the 4.2-5.2 Å region of the experimental signal.

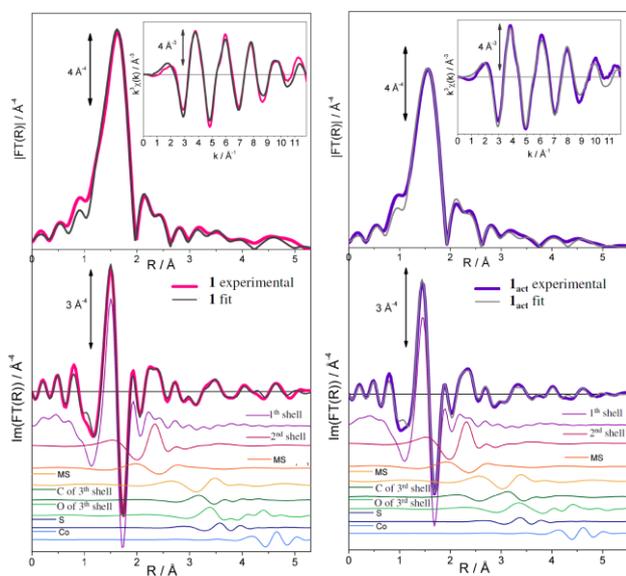


Figure 5. Comparison between experimental and corresponding EXAFS best fits for samples **1** and **1_{act}**, left and right panels, respectively. Top panels report the modulus of the FT (pink/purple lines for the experimental data, dark/light gray lines for the best fits), while bottom panels show the imaginary parts of the FT (same colour code used for the modulus), and the different paths contributions to the total signal. For quantitative values of the parameters optimized in the fits, see Table 1. The insets in the top panels report the fits in k -space.

Sample activation results in an overall contraction of the bond lengths determined by EXAFS, as clearly results by comparing the last two columns in Table 1. The first shell contracts by 0.050

± 0.009 Å, the Co(1)-S(1) distance by 0.18 ± 0.12 Å. The contraction of the Co(1)-Co(1#) distance is lower than the associated error: 0.05 ± 0.09 Å, but it can be taken as significant, since it follows the same trend. The errors associated to the second and third shell contributes of low Z neighbors are too large to appreciate any difference between samples **1** and **1_{act}**.

2.5. Porosity and CO₂ isotherm.

The presence of porosity was assessed through a volumetric gas uptake measurement, after a pre-activation treatment on **1** at 190 °C for 24 h. At the end of the activation process the material changes its color from purple (**1**) to blue (**1_{act}**, see below Figure 7a), proof of evidence of the dehydration on Co(II). The N₂ adsorption isotherm at 77 K (Figure S6) showed no inner surface area, the BET calculated value being only 6.13 m²/g. The isotherm shape is typical of a non-porous material. The same result was obtained using argon as adsorptive, at 87 K (final BET surface area = 1.46 m²/g, Figure S7). On the contrary, the interaction of the material with the polar carbon dioxide (CO₂) at 273 K and $p_{\max} = 920$ torr is significantly stronger: no plateau was reached at the maximum pressure (Figure 6), and a final value of 4.7 wt. % was calculated under the applied experimental conditions.

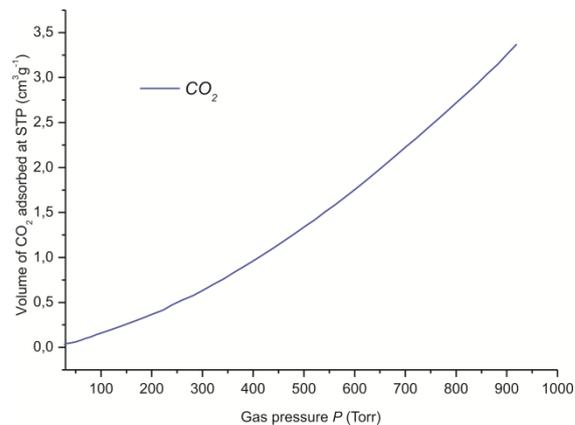


Figure 6. CO₂ adsorption isotherm (273 K) of **1_{act}**.

2.6. UV-Vis and IR study.

As already mentioned in the previous section, the purple colored sample **1** turns into a blue-violet powder upon activation at 190 °C (**1_{act}**, see insets of Figure 7a). As seen for several other MOFs,^{17,30,36} UV-Vis spectroscopy can be an useful technique to obtain additional information on the electronic structure (and the local coordination environment symmetry) of Co(II) in both **1** and **1_{act}**. In the $d-d$ region, Co(II) high-spin d^7 system in octahedral symmetry should be characterized by three spin allowed transitions: ${}^4T_{2g}(F) \leftarrow {}^4T_{1g}(F)$; ${}^4A_{2g}(F) \leftarrow {}^4T_{1g}(F)$ and ${}^4T_{1g}(P) \leftarrow {}^4T_{1g}(F)$ falling in the NIR (the first) and visible (the second and the third) regions, respectively. The presence of a distorted symmetry for Co(II) sites in **1** induces the appearance of more components, as clearly observed in Figure 7a. In particular, sample **1** (pink curve) shows a band at 1190 nm followed by a

complex absorption pattern in the form of a triplet at 614, 522 and 460 nm, respectively. At higher frequency, an additional band with Ligand-to-Metal Charge Transfer character is observed at around 245 nm. Upon dehydration (violet curve), the spectrum changes substantially. The distorted octahedral Co(II) sites move towards a coordination number decrease (from 6 to 5) and related symmetry change. A general intensity increase of all the bands is observed, in both the charge transfer and *d-d* regions. As for the CT band, this behaviour cannot find a simple explanation, while, in the case of the *d-d* features the experimental results can be explained in terms of a disruption of the O_h -like symmetry, in full agreement with the conclusions drawn from the XANES study (see above). In particular, the appearance of a clear triplet at 453, 570, 691 nm and a further component at 1430 nm, together with the intensity decrease and shift at 1090 nm of the 1190 nm band, indicate a symmetry lowering at the metal centre that causes the splitting of the ${}^4T_{2g}$ state associated to the *F* term. This behaviour can be better justified with an octahedral (O_h) to square pyramidal (C_{4v}) rather than octahedral to tetrahedral (T_d) coordination geometry change.

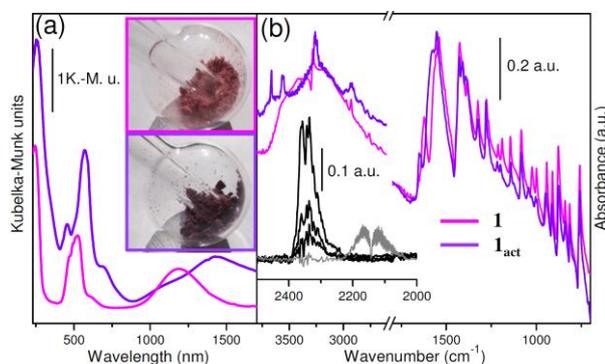


Figure 7. UV-Vis, part (a), and IR, part (b), of samples **1** (purple) and **1_{act}** (blue-violet). Insets in part (a) report the photographs of **1** (top) and **1_{act}** (bottom). The inset in part (b) reports the IR spectra, collected at RT, of CO ($P_{eq} = 100$ mbar) and CO₂ dosed on sample **1_{act}**, gray and black lines, respectively. For CO₂, three different equilibrium pressures are reported ($P_{eq} = 80, 40,$ and 20 mbar).

Figure 7b shows the evolution of the IR spectrum of **1** upon activation at 190 °C. From vibrational spectroscopy, the water removal is testified by the substantial decrease of the broad band centered at 3300 cm^{-1} and the component at 1622 cm^{-1} , due to $\nu_{\text{sym}}(\text{OH})$, $\nu_{\text{asym}}(\text{OH})$ and $\delta(\text{OH})$, respectively. **1_{act}** shows two sharp components at 3655 and at 3563 cm^{-1} that could be assigned to $\nu(\text{OH})$ of hydroxyl groups present in termination sites and defects of the structure. In the framework vibrational region no relevant changes are observed upon water removal: most of the sharp bands due to the vibration of the organic linkers are not strongly modified; only a slight shift in the maxima positions is observed. Bands involving directly the coordination of Co sites are too low in energy to be observed by using this experimental set up. The inset of Figure 7b reports the effect of interaction at RT with CO (grey curve, $P_{eq} = 100$ mbar) and CO₂ (black curves, $P_{eq} = 80, 40,$ and 20 mbar). In both cases, only the presence of gas phase is observed, testifying that both CO and CO₂ are not

specifically interacting with the surface sites of the material, in particular with the exposed Co(II) ions. Similar experiments performed on other porous coordination polymers showing accessible Co(II) sites gave bands around 2160 cm^{-1} and at 2341 cm^{-1} for CO and CO₂ respectively.³⁷

3. Conclusions

In summary, a new chiral Metal-Organic Framework has been synthesised starting from an enantiomerically pure thiazolidine-based carboxylate. The material has been fully characterized through a combination of X-ray diffraction (single crystal and powder) and spectroscopic (CD, UV-Vis, IR, XANES, EXAFS) techniques. The satisfactory CO₂ uptake at 273 K paves the way towards a possible application of this material as carbon dioxide sponge for Carbon Capture and Sequestration (CCS) technology. New thiazole and thiazolidine-based ligands are currently being synthesized in our laboratories with the aim of creating new tailor-made MOFs for this purpose.

4. Experimental Section

4.1. General considerations on the synthesis and on the X-ray structural refinement.

All starting materials and solvents were of analytical grade. They were purchased from Aldrich and used as received, without further purification. Thermal gravimetric analysis measurements were performed on an EXSTAR Thermo Gravimetric Analyzer (TG/DTA) Seiko 6200 under N₂ atmosphere (50 mL/min) coupled with a ThermoStar™ GSD 301 T (TGA-MS) for MS gas analysis of volatiles. Elemental analyses were performed using a Thermo FlashEA 1112 Series CHNS-O elemental analyzer with an accepted tolerance of ± 0.4 units. Adsorption isotherms were recorded using a Micromeritics® ASAP 2020 instrument. Prior to the measurements, the samples were degassed at the desired temperature using a heating rate of 5 °C min⁻¹ and holding that temperature for the chosen period of time. N₂ adsorption isotherms were recorded at 77 K, using a liquid nitrogen bath. Ar adsorption isotherms were recorded at 87 K, using a liquid argon bath. CO₂ adsorption isotherms were recorded at 273 K, using an ice bath. Single crystal X-ray data were collected at low temperature (100 K) on an Oxford Diffraction XCALIBUR 3 diffractometer equipped with a CCD area detector using Mo K α radiation ($\lambda = 0.7107$ Å). The program used for the data collection was CrysAlis CCD 1.171.³⁸ Data reduction was carried out with the program CrysAlis RED 1.171³⁹ and the absorption correction was applied with the program ABSPACK 1.17. Direct methods implemented in Sir97⁴⁰ were used to solve the structures and the refinements were performed by full-matrix least-squares against F^2 implemented in SHELX97.⁴¹ All the non-hydrogen atoms were refined anisotropically while the hydrogen atoms (except for those of the crystallization water molecule in **1**, which could not be located on the Fourier difference density maps) were fixed in calculated positions and refined isotropically with the thermal factor depending on the one of the atom to which they are bound. The geometrical calculations were performed by PARST97⁴² and molecular plots were produced by the program

ORTEP3.⁴³ X-ray powder diffraction (XRPD) measurements were carried out with a Panalytical® X'PERT PRO powder diffractometer equipped with a diffracted beam Ni filter and an PIXcel® solid state detector in the $4 \div 75^\circ 2\theta$ region, operating with CuK α radiation ($\lambda = 1.54 \text{ \AA}$). Anti-scatter slits were used both on the incident (0.25° and 0.5° divergence) and the diffracted (7.5 mm height) beam. The 2θ step size was 0.03° , with a counting time of 60 s/step . Variable temperature (VT) X-ray powder diffraction patterns were collected in the $25 \div 250^\circ \text{C}$ temperature range using an Anton Paar HTK 1200N Oven camera. The measurements were carried out at ambient pressure under a mild N₂ flow. CD spectra were measured using a Jasco J-715 Spectropolarimeter. Deuterated solvents for routine NMR measurements were dried over molecular sieves. ¹H NMR spectra were recorded operating at 300.0 and 400.0 MHz ; ¹³C{¹H} NMR spectra were recorded operating at 75.48 and 100.61 MHz . Peak positions are relative to tetramethylsilane and were calibrated against the residual solvent resonance. Coupling constants (J) are reported in Hz. Ordinary FT-IR spectra of the H₂L ligands were recorded in KBr pellets. Elemental combustion microanalyses (C, H, N) were obtained using an elemental analyzer. ESI-MS spectra of H₂L ligands were done on a LCQ Orbitrap mass spectrometer equipped with a conventional ESI source by direct injection of the sample solution. 80 scans were accumulated and averaged for each spectrum.

4.2. X-ray absorption data collection and EXAFS data analysis

X-ray absorption experiments, at the Co K-edge (7709 eV), were performed at the BM26A of the ESRF facility (Grenoble, F).⁴⁴ The white beam was monochromatized using a Si(111) double crystal; harmonic rejection was performed by detuning the crystals at 20% of the rocking curve. The following experimental geometry was adopted: 1) I₀ (N₂ 0.15 atm and He 0.85 atm , resulting in an overall efficiency of 10%); 2) MOF sample; 3) I₁ (N₂ 0.70 atm , He 0.30 atm , resulting in an overall efficiency of 50%); 4) reference Co foil; 5) I₂ (80% efficiency). This set-up allows a direct energy/angle calibration for each spectrum avoiding any problem related to little energy shifts due to small thermal instability of the monochromator crystals.⁴⁵ The sample was prepared in the form of a self supported pellet, with the thickness optimized to obtain an edge jump of $\Delta\mu_x = 1.0$, with an absolute absorption after the edge of μ_x of ca. 1.5 . The pellet was activated and measured inside an *ad hoc* conceived cell that allows, evacuation, gas dosage and warming and cooling.⁴⁶ The pre-edge region was acquired with an energy step of 10 eV and an integration time of 1 s/point . The edge region was collected using an energy step of 0.2 eV and an integration time of 5 s/point . The EXAFS part of the spectra was collected with a variable sampling step in energy, resulting in a constant sampling step in k-space of $\Delta k = 0.05 \text{ \AA}^{-1}$, up to 18 \AA^{-1} , with an integration time that linearly increases with k from 5 to 25 s/point to account for the low signal-to-noise ratio at high k values. The extraction of the $\chi(k)$ function was performed using Athena program⁴⁷ in the $\Delta k = 2.0\text{-}11.8 \text{ \AA}^{-1}$ interval. For the pristine (**1**) and activated (**1_{act}**) samples, two consecutive EXAFS spectra were collected, resulting in two μ_x spectra, and corresponding $\chi(k)$ functions

were averaged before data analysis as described elsewhere.⁴⁸

EXAFS data analysis has been performed using the Artemis software.⁴⁷ Phase and amplitude functions were calculated by FEFF6 code⁴⁹ using as input a cluster obtained from the single crystal XRD refinement and including all atoms included within a sphere of radius 5.5 \AA centered in the absorbing Co atom. Figure 4d evidences the atoms included in the cluster (see Figure S8 of the ESI for a larger view of the cluster embedded in the MOF framework). The fits were performed in R-space in the $\Delta R = 1.00\text{-}5.20 \text{ \AA}$ range resulting in 26 independent points ($2\Delta k\Delta R/\pi > 26$). Due to the complexity of the structure, many single scattering (SS) and multiple scattering (MS) paths contribute to the overall EXAFS signal. Excluding the paths having an amplitude smaller than 10% of the most intense one (the Co–O SS of the first shell), more than 50 paths were included in the fit. To limit the number of optimized variables, all paths have been optimized with the same amplitude factor (S_0^2) and with the same energy shift parameter (ΔE). Moreover, considering the atomic species and distance ranges, different shells of atoms around the Co absorber were defined and for each shell the same parameters (Debye-Waller factor and ΔR) were used to simulate the SS paths.

4.3. UV-Vis and IR spectroscopies.

UV-Vis-NIR spectra collected on both **1** and **1_{act}** were performed using a Cary 5000 spectrophotometer, equipped with a reflectance sphere and a tailor-made cell allowing for the data collection under controlled atmosphere on activated samples. FTIR spectra were collected in transmission mode on self-supporting wafer under controlled atmosphere. The spectra were recorded at 2 cm^{-1} resolution on a Bruker IFS 66 FTIR spectrometer, equipped with a MCT detector.

4.4. CD measurements on H₂L and **1**.

CD spectra for the ligands (**H₂L-RR** and **H₂L-SR**) were recorded on 9.1 mM water solutions using a 0.1 cm cell. CD spectra for the polymer were recorded on microcrystalline samples using the technique of KCl pellet as follows.⁵⁰ Less than 1 mg of the crystalline polymer was mixed with $\approx 100 \text{ mg}$ of oven-dried KCl, finely ground and pressed at $\approx 7 \text{ kbar}$ under vacuum for 15 min to produce a glassy translucent disc. Several different samples were prepared to assure reproducibility. The pellet was mounted on a rotatable support placed as close as possible to the detector. On each sample, several CD spectra were measured upon rotation of the disk around the incident axis direction and 180° -flip around the vertical. These spectra were almost superimposable to each other, demonstrating the absence of detectable spectral artefacts.⁵⁰

4.5. Preparation of [Co(L-RR)(H₂O) • H₂O]₆ (**1**).

Cobalt(II) chloride hexahydrate CoCl₂ • 6H₂O (1.10 g , 4.6 mmol) and **H₂L-RR** (0.41 g , 2.3 mmol) were dissolved in 7 mL of deionized water. The resulting clear purple solution was transferred to a Teflon-lined stainless steel autoclave, sealed and heated under autogeneous pressure at 90°C for 24 h . After slow overnight cooling, purple crystals of **1** were collected, washed

with fresh ethanol (4 x 10 mL), petroleum ether (4 x 10 mL) and finally dried under a nitrogen stream at room temperature. Yield: 0.065 g (10.5 %, calculated with respect to the ligand). The phase purity was checked through XRPD, comparing the experimental diffractogram with that calculated from the single-crystal structure. Anal. Calcd. for **1**, C₅H₉CoNO₆S (270.13): C, 22.23; H, 3.36; N, 5.19; S, 11.87. Found: C, 21.57; H, 2.69; N, 5.00; S, 11.68. IR bands (KBr, cm⁻¹) for **1**: 3421 m,br [ν(O-H)]; 3287 s [ν(N-H)]; 2930 m [ν(C-H)]; 1613 s,sh and 1560 vs [ν(COO⁻)]; 1430 s [δ(H-O-H)].

Acknowledgments

The *motu proprio* FIRENZE HYDROLAB project by Ente Cassa di Risparmio di Firenze (<http://www.iccom.cnr.it/hydrolab/>) and the PIRODE project by MATTM (Rome) are kindly acknowledged for funding this research activity through a postdoctoral grant to B.D.C.

²⁰ *Istituto di Chimica dei Composti Organometallici (ICCOM - CNR), Via Madonna del Piano 10, 50019, Sesto Fiorentino (Italy). E-mail: a.rossin@iccom.cnr.it*

^b *Dipartimento di Chimica e Chimica Industriale, Università di Pisa, via Risorgimento 35, 56126 Pisa, Italy.*

²⁵ *Department of Inorganic, Physical and Materials Chemistry, INSTM Reference Center and NIS Centre of Excellence, Università di Torino, Via Quarello 11, I-10135 Torino, Italy.*

† Electronic Supplementary Information (ESI) available: scheme of the diastereomeric enrichment of **H₂L**; CD spectra of (**2R,4R**)-**H₂L** and (**2S,4R**)-**H₂L**; PXRD patterns for **1** and **1_{act}**; crystallographic data and tables for **1**, TG-DTG and related MS spectra of **1**; VT-PXRD spectra of **1**; N₂ and Ar adsorption isotherms recorded at 77 K and 87 K (respectively) on **1_{act}**; cluster of the local environment of Co(II) used to calculate phases and amplitudes of the different SS and MS paths contributing to the EXAFS signal. Additional details on the EXAFS data analysis. The crystallographic data for **1** have been deposited (CCDC Number 855629).

⁴⁰ See DOI: 10.1039/b000000x/

References

- (a) For a general survey on MOFs, see the themed issue: *Chem. Soc. Rev.*, 2009, **38**, 1201-1508, and references therein. (b) D. Zhao, D. J. Timmons, D. Q. Yuan and H. C. Zhou, *Acc. Chem. Res.*, 2011, **44**, 123-133.
- (a) S. L. Qiu and G. S. Zhu, *Coord. Chem. Rev.*, 2009, **253**, 2891-2911. (b) L. Q. Ma, C. D. Wu, M. M. Wanderley and W. B. Lin, *Angew. Chem.-Int. Ed.*, 2010, **49**, 8244-8248. (c) Y. Liu, W. M. Xuan and Y. Cui, *Adv. Mater.*, 2010, **22**, 4112-4135.
- B. Gil-Hernandez, H. A. Hoppe, J. K. Vieth, J. Sanchiz and C. Janiak, *Chem. Commun.*, 2010, **46**, 8270-8272.
- X. M. Jing, L. R. Zhang, T. L. Ma, G. H. Li, Y. Yu, Q. S. Huo, M. Eddaoudi and Y. L. Liu, *Cryst. Growth Des.*, 2010, **10**, 492-494.
- A. Mallick, S. Saha, P. Pachfule, S. Roy and R. Banerjee, *J. Mater. Chem.*, 2010, **20**, 9073-9080.
- (a) L. E. Gordon and W. T. A. Harrison, *Inorg. Chem.*, 2004, **43**, 1808-1809. (b) E. V. Anokhina and A. J. Jacobson, *J. Am. Chem. Soc.*, 2004, **126**, 3044-3045.
- J. B. Weng, M. C. Hong, Q. Shi, R. Cao and A. S. C. Chan, *Eur. J. Inorg. Chem.*, 2002, 2553-2556.
- (a) J. Fan, C. Slebodnick, R. Angel and B. E. Hanson, *Inorg. Chem.*, 2005, **44**, 552-558. (b) L. Chen and X. H. Bu, *Chem. Mater.*, 2006, **18**, 1857-1860.
- M. Mizutani, N. Maejima, K. Jitsukawa, H. Masuda and H. Einaga, *Inorganica Chimica Acta*, 1998, **283**, 105-110.
- (a) S. Thushari, J. A. K. Cha, H. H. Y. Sung, S. S. Y. Chui, A. L. F. Leung, Y. F. Yen and I. D. Williams, *Chem. Commun.*, 2005, 5515-5517. (b) A. S. F. Au-Yeung, H. H. Y. Sung, J. A. K. Cha, A. W. H. Siu, S. S. Y. Chui and I. D. Williams, *Inorg. Chem. Commun.*, 2006, **9**, 507-511.
- Y. K. Lv, C. H. Zhan, Z. G. Jiang and Y. L. Feng, *Inorg. Chem. Commun.*, 2010, **13**, 440-444.
- K. Gedrich, I. Senkowska, I. A. Baburin, U. Mueller, O. Trapp and S. Kaskel, *Inorg. Chem.*, 2010, **49**, 4440-4446.
- F. J. Song, C. Wang, J. M. Falkowski, L. Q. Ma and W. B. Lin, *J. Am. Chem. Soc.*, 2010, **132**, 15390-15398.
- (a) J. S. Seo, D. Whang, H. Lee, S. I. Jun, J. Oh, Y. J. Jeon and K. Kim, *Nature*, 2000, **404**, 982-986. (b) S. Kitagawa, R. Kitaura and S. Noro, *Angew. Chem.-Int. Ed.*, 2004, **43**, 2334-2375. (c) S. J. Lee and W. B. Lin, *Acc. Chem. Res.*, 2008, **41**, 521-537. (d) G. A. Hembury, V. V. Borovkov and Y. Inoue, *Chem. Rev.*, 2008, **108**, 1-73.
- (a) A. Corma, H. Garcia and F. X. Llabres i Xamena, *Chem. Rev.*, 2010, **110**, 4606-4655. (b) D. B. Dang, P. Y. Wu, C. He, Z. Xie and C. Y. Duan, *J. Am. Chem. Soc.*, 2010, **132**, 14321-14323. (c) W. B. Lin, *Top. Catal.*, 2010, **53**, 869-875. (d) F. J. Song, C. Wang and W. B. Lin, *Chem. Commun.*, 2011, **47**, 8256-8258. (e) K. S. Jeong, Y. B. Go, S. M. Shin, S. J. Lee, J. Kim, O. M. Yaghi and N. Jeong, *Chem. Sci.*, 2011, **2**, 877-882.
- B. Di Credico, G. Reginato, L. Gonsalvi, M. Peruzzini and A. Rossin, *Tetrahedron*, 2011, **67**, 267-274.
- (a) K. C. Szeto, K. P. Lillerud, M. Tilset, M. Bjorgen, C. Prestipino, A. Zecchina, C. Lamberti and S. Bordiga, *J. Phys. Chem. B*, 2006, **110**, 21509-21520. (b) K. C. Szeto, C. Prestipino, C. Lamberti, A. Zecchina, S. Bordiga, M. Bjorgen, M. Tilset and K. P. Lillerud, *Chem. Mater.*, 2007, **19**, 211-220. (c) J. Hafizovic, M. Bjorgen, U. Olsbye, P. D. C. Dietzel, S. Bordiga, C. Prestipino, C. Lamberti and K. P. Lillerud, *J. Am. Chem. Soc.*, 2007, **129**, 3612-3620. (d) J. H. Cavka, S. Jakobsen, U. Olsbye, N. Guillou, C. Lamberti, S. Bordiga and K. P. Lillerud, *J. Am. Chem. Soc.*, 2008, **130**, 13850-13851. (e) N. Masciocchi, S. Galli, V. Colombo, A. Maspero, G. Palmisano, B. Seyyedi, C. Lamberti and S. Bordiga, *J. Am. Chem. Soc.*, 2010, **132**, 7902-7904. (f) S. Bordiga, F. Bonino, K. P. Lillerud and C. Lamberti, *Chem. Soc. Rev.*, 2010, **39**, 4885-4927. (g) L. Valenzano, B. Civalieri, S. Bordiga, M. H. Nilsen, S. Jakobsen, K.-P. Lillerud and C. Lamberti, *Chem. Mater.*, 2011, **23**, 1700-1718. (h) S. Chavan, J. G. Vitillo, D. Gianolio, O. Zavorotynska, B. Civalieri, S. Jakobsen, M. H. Nilsen, L. Valenzano, C. Lamberti, K. P. Lillerud and S. Bordiga, *Phys. Chem. Chem. Phys.*, 2012, in press. DOI:10.1039/C1031CP23434J.
- (a) O. R. Evans, D. R. Manke and W. B. Lin, *Chem. Mater.*, 2002, **14**, 3866-3874. (b) X. W. Wang, L. Han, T. J. Cai, Y. Q. Zheng, J. Z. Chen and Q. Deng, *Cryst. Growth Des.*, 2007, **7**, 1027-1030. (c) H. Y. Liu, B. Zhao, W. Shi, Z. J. Zhang, P. Cheng, D. Z. Liao and S. P. Yan, *Eur. J. Inorg. Chem.*, 2009, 2599-2602. (d) S. M. Chen, J. Zhang and X. H. Bu, *Inorg. Chem.*, 2009, **48**, 6356-6358. (e) Q. L. Zhu, T. L. Sheng, R. B. Fu, C. H. Tan, S. M. Hu and X. T. Wu, *Chem. Commun.*, 2010, **46**, 9001-9003. (f) X. L. Zhao, H. Y. He, F. N. Dai, D. F. Sun and Y. X. Ke, *Inorg. Chem.*, 2010, **49**, 8650-8652. (g) A. C. Kathalikkattil, P. S. Subramanian and E. Suresh, *Inorg. Chim. Acta*, 2011, **365**, 363-370.
- (a) R. Kuroda and T. Honma, *Chirality*, 2000, **12**, 269-277. (b) R. Kuroda, in *Circular dichroism: principles and applications*, 2nd ed., eds. N. Berova, K. Nakanishi and R. W. Woody, Wiley-VCH, New York, 2000, pp. 159-184.
- G. Pescitelli, T. Kurtan, U. Florke and K. Krohn, *Chirality*, 2009, **21**, E181-E201.
- A. Rossin, B. Di Credico, G. Giambastiani, L. Gonsalvi, M. Peruzzini and G. Reginato, *Eur. J. Inorg. Chem.*, 2011, 539-548.

- 22 (a) W. P. Liao, C. Liu, X. F. Wang, G. S. Zhu, X. J. Zhao and H. J. Zhang, *CrystEngComm*, 2009, **11**, 2282-2284 (b) S. Paranthaman, F. X. Coudert and A. H. Fuchs, *Phys. Chem. Chem. Phys.*, 2010, **12**, 8123-8129. (c) Y. F. Chen, J. Y. Lee, R. Babarao, J. Li and J. W. Jiang, *J. Phys. Chem. C*, 2010, **114**, 6602-6609.
- 23 Crystallographic parameters for **2**: tetragonal, $P 4_1$, $a = b = 12.333(3)$ Å; $c = 5.284(2)$ Å. $V_{\text{cell}} = 803.77(7)$ Å³.
- 24 T. Pakkanen and T. Pakkanen, *Acta Cryst. B*, 1979, **35**, 2670-2672.
- 25 For a comprehensive review on MOFs with exposed metal sites see, M. Dinca and J. R. Long, *Angew. Chem.-Int. Ed.*, 2008, **47**, 6766-6779.
- 26 S. Q. Ma and H. C. Zhou, *J. Am. Chem. Soc.*, 2006, **128**, 11734-11735.
- 27 (a) S. Mason, *Molecular Optical Activity and the Chiral Discrimination*, Cambridge University Press, Cambridge, 1982. (b) R. Kuroda and Y. Saito, in *Circular dichroism: principles and applications*, 2nd ed., eds. N. Berova, K. Nakanishi and R. W. Woody, Wiley-VCH, New York, 2000, pp. 563-599.
- 28 (a) J. Bolard and G. Chottard, *J. Inorg. Nucl. Chem.*, 1974, **36**, 1677-1682. (b) H. Miyake, M. Hikita, M. Itazaki, H. Nakazawa, H. Sugimoto and H. Tsukube, *Chem.-Eur. J.*, 2008, **14**, 5393-5396. (c) S. L. Liang, Z. L. Liu, C. M. Liu, X. W. Di, J. Zhang and D. Q. Zhang, *Z. Anorg. Allg. Chem.*, 2009, **635**, 549-553.
- 29 J. Reedijk, W. L. Driessen and W. L. Groeneveld, *Rec. Trav. Chim. Pays-Bas*, 1969, **88**, 1095-1109.
- 30 (a) F. Bonino, S. Chavan, J. G. Vitillo, E. Groppo, G. Agostini, C. Lamberti, P. D. C. Dietzel, C. Prestipino and S. Bordiga, *Chem.Mater.*, 2008, **20**, 4957-4968. (b) S. Chavan, F. Bonino, J. G. Vitillo, E. Groppo, C. Lamberti, P. D. C. Dietzel, A. Zecchina and S. Bordiga, *Phys. Chem. Chem. Phys.*, 2009, **11**, 9811-9822. (c) S. Chavan, J. G. Vitillo, E. Groppo, F. Bonino, C. Lamberti, P. D. C. Dietzel and S. Bordiga, *J. Phys. Chem. C*, 2009, **113**, 3292-3299.
- 31 (a) V. Bolis, S. Bordiga, C. Lamberti, A. Zecchina, A. Carati, F. Rivetti, G. Spano and G. Petrini, *Langmuir*, 1999, **15**, 5753-5764. (b) G. Berlier, G. Spoto, S. Bordiga, G. Ricchiardi, P. Fiscaro, A. Zecchina, I. Rossetti, E. Selli, L. Forni, E. Giamello and C. Lamberti, *J. Catal.*, 2002, **208**, 64-82. (c) E. Groppo, C. Prestipino, F. Cesano, F. Bonino, S. Bordiga, C. Lamberti, P. C. Thüne, J. W. Niemantsverdriet and A. Zecchina, *J. Catal.*, 2005, **230**, 98-108. (d) S. Bordiga, F. Bonino, A. Damin and C. Lamberti, *Phys. Chem. Chem. Phys.*, 2007, **9**, 4854-4878.
- 32 (a) C. Prestipino, G. Berlier, F. X. Llabrés i Xamena, G. Spoto, S. Bordiga, A. Zecchina, G. T. Palomino, T. Yamamoto and C. Lamberti, *Chem. Phys. Lett.*, 2002, **363**, 389-396. (b) F. X. Llabrés i Xamena, P. Fiscaro, G. Berlier, A. Zecchina, G. T. Palomino, C. Prestipino, S. Bordiga, E. Giamello and C. Lamberti, *J. Phys. Chem. B*, 2003, **107**, 7036-7044. (c) C. Prestipino, P. L. Solari and C. Lamberti, *J. Phys. Chem. B*, 2005, **109**, 13132-13137. (d) C. Prestipino, L. Capello, F. D'Acapito and C. Lamberti, *Phys. Chem. Chem. Phys.*, 2005, **7**, 1743-1746.
- 33 J. A. Bearden and A. F. Burr, *Rev. of Mod. Phys.* 1967, **39**, 125.
- 34 (a) P. Glatzel and U. Bergmann, *Coord. Chem. Rev.*, 2005, **249**, 65-95. (b) P. Glatzel, M. Sikora, G. Smolentsev and M. Fernandez-Garcia, *Catal. Today*, 2009, **145**, 294-299. (c) J. Singh, C. Lamberti and J. A. van Bokhoven, *Chem. Soc. Rev.*, 2010, **39**, 4754-4766. (d) J. C. Swarbrick, Y. Kvashnin, K. Schulte, K. Seenivasan, C. Lamberti and P. Glatzel, *Inorg. Chem.*, 2010, **49**, 8323-8332.
- 35 C. Prestipino, L. Regli, J. G. Vitillo, F. Bonino, A. Damin, C. Lamberti, A. Zecchina, P. L. Solari, K. O. Kongshaug and S. Bordiga, *Chem. Mater.*, 2006, **18**, 1337-1346.
- 36 S. Bordiga, C. Lamberti, G. Ricchiardi, L. Regli, F. Bonino, A. Damin, K. P. Lillerud, M. Bjorgen and A. Zecchina, *Chem. Commun.*, 2004, 2300-2301.
- 37 S. Chavan, *Characterization of Metal-organic Frameworks for Gas Storage and Catalysis applications*, Ph.D. thesis in materials science, University of Torino (I), 2010.
- 38 CrysAlisCCD 1.171.31.2 (release 07-07-2006), CrysAlis171 .NET, Oxford Diffraction Ltd.
- 39 CrysAlis RED 1.171.31.2 (release 07-07-2006), CrysAlis171 .NET, Oxford Diffraction Ltd.
- 40 A. Altomare, M. C. Burla, M. Camalli, G. L. Cascarano, C. Giacovazzo, A. Guagliardi, A. G. G. Moliterni, G. Polidori and R. Spagna, *J. Appl. Crystallogr.*, 1999, **32**, 115-119.
- 41 (a) G. M. Sheldrick, *Acta Cryst. A*, 2008, **64**, 112-122. (b) G. M. Sheldrick, *Acta Cryst. D-Biol. Crystallogr.*, 2010, **66**, 479-485.
- 42 M. Nardelli, *Comput. Chem.*, 1983, **7**, 95-98.
- 43 L. Farrugia, *J. Appl. Crystallogr.*, 1997, **30**, 565.
- 44 (a) S. Nikitenko, A. M. Beale, A. M. J. van der Eerden, S. D. M. Jacques, O. Leynaud, M. G. O'Brien, D. Detollenaere, R. Kaptein, B. M. Weckhuysen and W. Bras, *J. Synchrot. Radiat.*, 2008, **15**, 632-640. (b) G. Silversmit, B. Vekemans, S. Nikitenko, W. Bras, V. Czech, G. Zaray, I. Szaloki and L. Vincze, *J. Synchrot. Radiat.*, 2009, **16**, 237-246.
- 45 C. Lamberti, S. Bordiga, F. Bonino, C. Prestipino, G. Berlier, L. Capello, F. D'Acapito, F. X. L. I. Xamena and A. Zecchina, *Phys. Chem. Chem. Phys.*, 2003, **5**, 4502-4509.
- 46 C. Lamberti, C. Prestipino, S. Bordiga, G. Berlier, G. Spoto, A. Zecchina, A. Laloni, F. La Manna, F. D'Anca, R. Felici, F. D'Acapito and P. Roy, *Nucl. Instrum. Meth. B*, 2003, **200**, 196-201.
- 47 B. Ravel and M. Newville, *J. Synchrot. Radiat.*, 2005, **12**, 537-541.
- 48 C. Lamberti, S. Bordiga, D. Arduino, A. Zecchina, F. Geobaldo, G. Spanò, F. Genoni, G. Petrini, A. Carati, F. Villain and G. J. Vlaic, *Phys. Chem. B*, 1998, **102**, 6382-6390.
- 49 S. I. Zabinsky, J. J. Rehr, A. Ankudinov, R. C. Albers and M. J. Eller, *Phys. Rev. B*, 1995, **52**, 2995-3009.
- 50 G. Pescitelli, T. Kurtan, U. Florke and K. Krohn, *Chirality*, 2009, **21**, E181-E201.

Synthesis, characterization and CO₂ uptake of a chiral Co(II) Metal-Organic Framework containing a thiazolidine-based spacer

*Andrea Rossin,^{*a} Barbara Di Credico,^a Giuliano Giambastiani,^a Maurizio Peruzzini,^{*a} Gennaro Pescitelli,^b Gianna Reginato,^a Elisa Forfecchia,^c Diego Gianolio,^c Carlo Lamberti,^c Silvia Bordiga^c*

^aIstituto di Chimica dei Composti Organometallici (ICCOM - CNR), Via Madonna del Piano 10, 50019, Sesto Fiorentino, (Italy)

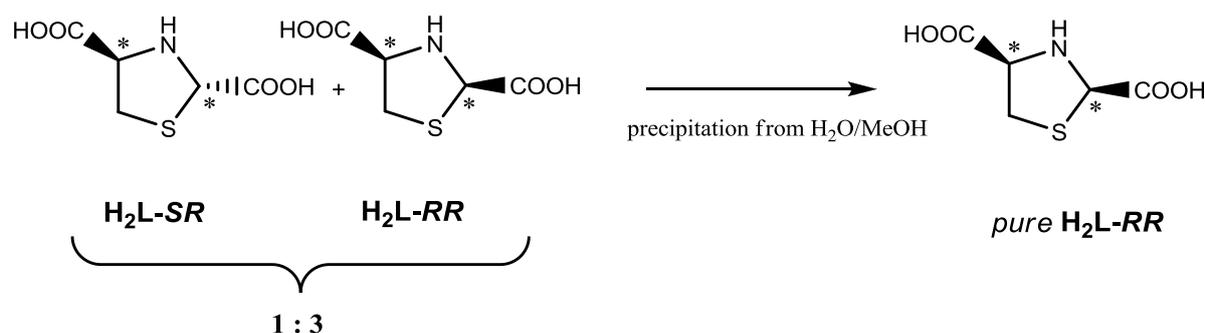
^b Dipartimento di Chimica e Chimica Industriale, Università di Pisa, via Risorgimento 35, 56126 Pisa, Italy.

^c Dipartimento di Chimica IFM and NIS Centre of Excellence, Università di Torino, INSTM UdR Università, Via Pietro Giuria 7, 10125 Torino, Italy

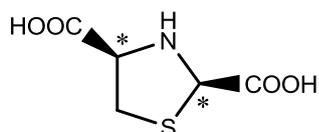
Electronic Supplementary Information

Preparation of H_2L and resolution of (2*R*,4*R*)-thiazolidine-2,4-dicarboxylic acid (H_2L -*RR*) and (2*S*,4*R*)-thiazolidine-2,4-dicarboxylic acid (H_2L -*SR*).

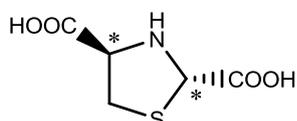
Diethyl thiazolidine-2(*R,S*),4(*R*)-dicarboxylate (4.0 g, 17.0 mmol)^[S1] was dissolved in MeOH (170.0 mL). A solution of cesium carbonate (22.20 g, 68.0 mmol) in H₂O (170.0 mL) was added and the mixture was stirred at room temperature overnight. The reaction mixture was then concentrated *in vacuo* to remove methanol. The aqueous phase was washed with ethyl acetate and acidified with concentrated HCl ($1 \leq \text{pH} \leq 4$), to let H_2L gradually precipitate out of the solution. The solid was collected by filtration, washed with EtOH (3 x 15 mL), H₂O (3 x 15mL) and Et₂O (3 x 15mL) to afford 3.0 g (100%) of H_2L as a white solid. The diastereoisomeric mixture was separated by successive crystallizations from H₂O/MeOH.



Scheme S1. Diastereomeric enrichment of H_2L .



H_2L -*RR*: IR (KBr, cm^{-1}): $\tilde{\nu} = 3295$ (NH), 1682 (CO). ¹H NMR (300 MHz, DMSO-*d*₆, 25 °C): δ 4.88 (s, 1H); 3.82 (dd, ABX spin system, $J_{AB} = 6.0$, $J_{BX} = 10.0$ Hz, 1H); 3.31 (dd, ABX spin system, $J_{AX} = 10.0$, $J_{AB} = 6.0$ Hz, 1H); 2.74-2.67 (bt, $J_{\text{app}} = 6.0$ Hz, 1H). ¹³C {¹H} NMR (75 MHz, DMSO-*d*₆, 25 °C): δ 172.53; 65.89; 55.38; 37.43. ESI-MS, m/z (%): 177(2) [M^+]. Anal. Calcd for C₅H₇NO₄S (177.18): C, 33.89; H, 3.98; N, 7.91. Found: C, 33.84; H, 4.00; N, 7.89.



H₂L-SR: IR (KBr, cm⁻¹): $\tilde{\nu}$ = 3295 (NH), 1684 (CO). ¹H NMR (300 MHz, DMSO-d₆, 25 °C): δ 4.88 (s, 1H); 4.24-4.19 (bt, J_{app} = 6.0 Hz, 1H); 3.14 (dd, ABX spin system, J_{AB} = 6.0, J_{BX} = 10.0 Hz, 1H); 2.90 (dd, ABX spin system, J_{AX} = 10.0, J_{AB} = 6.0 Hz, 1H). ¹³C {¹H} NMR (75 MHz, DMSO-d₆, 25 °C): δ 172.53; 65.89; 55.38; 37.43. ESI-MS, *m/z* (%): 177(2) [M⁺]. Anal. Calcd for C₅H₇NO₄S (177.18): C, 33.89; H, 3.98; N, 7.91. Found: C, 33.86; H, 3.95; N, 7.93.

Thiazolidine-2,4-dicarboxylic acid was prepared by condensation of cysteine with ethyl glyoxalate in aqueous methanol containing potassium bicarbonate and obtained as a 3:1 (*R,R*)/(*S,R*) diastereomeric mixture. Condensation reactions with aldehydes gave mixtures of two diastereoisomers, in 1:1 to 1:3 diastereomeric ratio, due to the presence of a new stereogenic centre generated at the C-2 atom of the thiazolidine ring. Ester saponification with Cs₂CO₃ in aqueous methanol afforded the corresponding carboxythiazoles, which were isolated after crystallization from acidic water and (remarkably) obtained as pure isomers after fractional crystallization from MeOH/H₂O.

The two diastereomers **H₂L-RR** and **H₂L-SR** had similar UV absorption spectra consisting of a broad band with a maximum at 245 nm in H₂O. More interestingly, the two electronic CD spectra had also similar shapes but mirror image-like appearance (Figure S1). Thus, the CD spectrum of the (*2R,4R*) diacid shows two negative bands with maxima at 250 and 213 nm followed by a positive high-energy tail, while the opposite signs are observed for the corresponding bands of the (*2S,4R*) diacid. The observed CD bands are likely to be allied with transitions centered on the sulfide moiety, as chiral sulfides show three distinct CD bands in the 200-240 nm region.^[S2] Therefore, it is conceivable that the chiral center closest to the sulfide group will contribute in a larger extent to the observed CD spectrum. In fact, the two diastereomers, differing in the configuration at C-2, show CD bands in similar positions but with opposite sign.

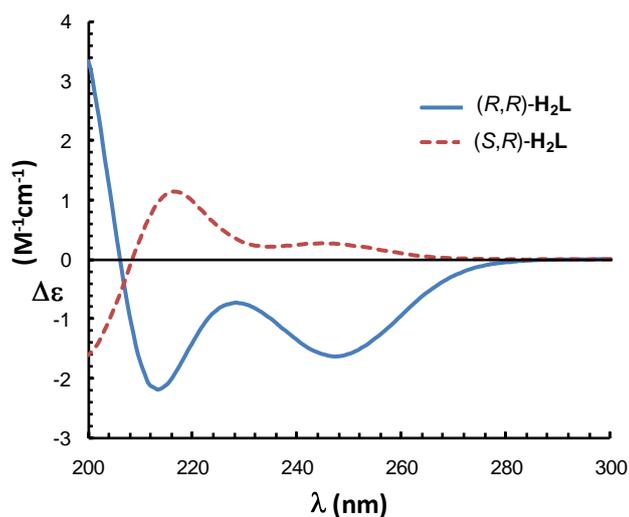


Figure S1. CD spectra of $(2R,4R)\text{-H}_2\text{L}$ and $(2S,4R)\text{-H}_2\text{L}$ (solid line: R,R diastereomer; dashed line: S,R diastereomer), 9.1 mM in H_2O ; 0.1 cm cell.

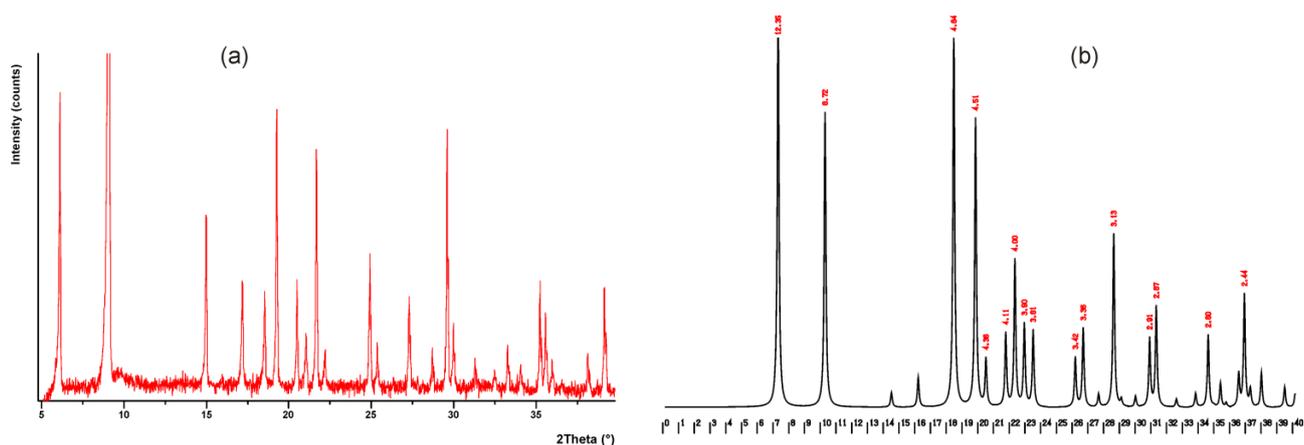
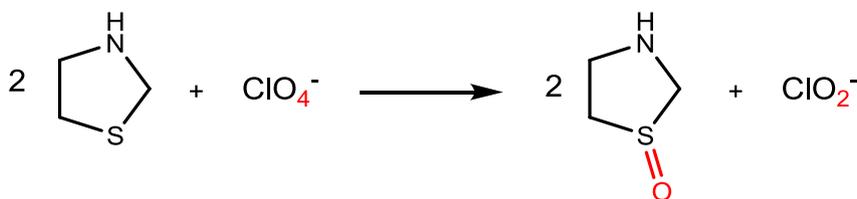


Figure S2. (a) Experimental and (b) simulated powder X-ray diffractogram of **1**. The red numbers on the simulated pattern indicate the corresponding d -spacing. The experimental peak intensity at $2\theta = 9^\circ$ is out of scale.



Scheme S2. Formation of the chlorite anion as a result of a redox reaction between the thiazolidine ring and perchlorate salts.

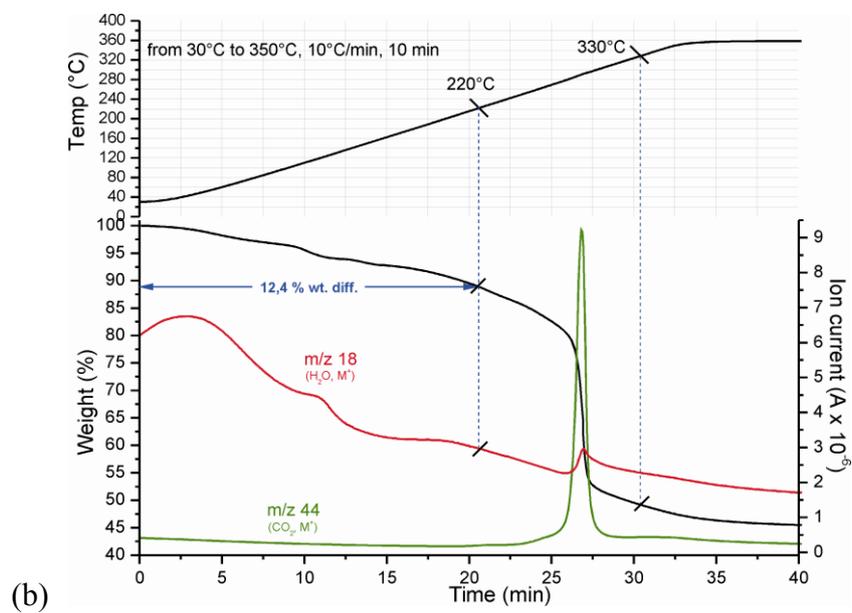
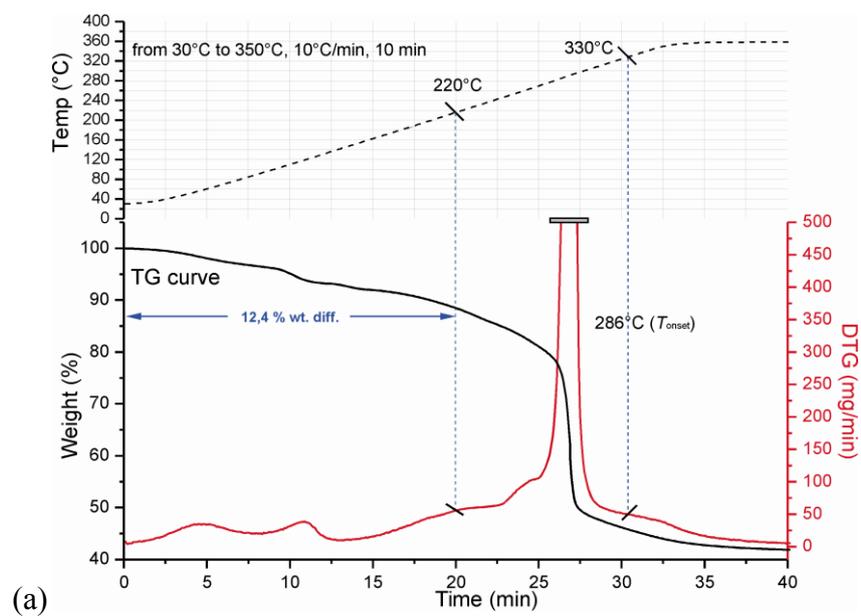


Figure S3. (a) TG-DTG and (b) related MS spectra of 1.

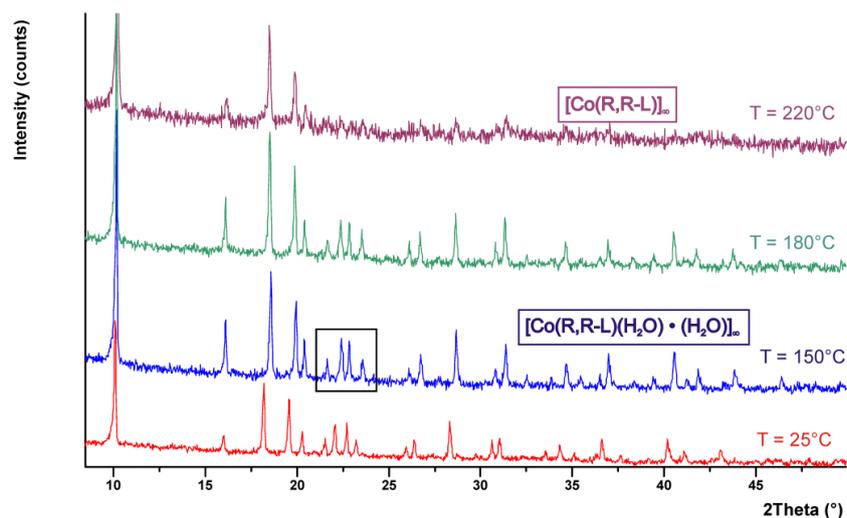


Figure S4. VT-PXRD spectra of **1**. The black square indicates the peaks that disappear upon dehydration, occurring between 180 and 220 °C. Compare with Figures S2(b) and S3.

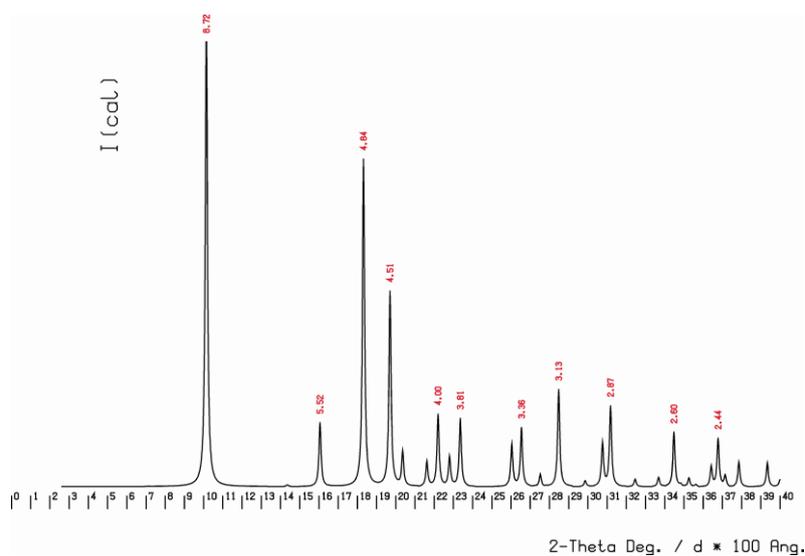


Figure S5. PXRD simulated pattern of the anhydrous $[\text{Co}(\text{L-RR})]_{\infty}$ phase (**1_{act}**) built from the single crystal data. Compare with Figure S2(b).

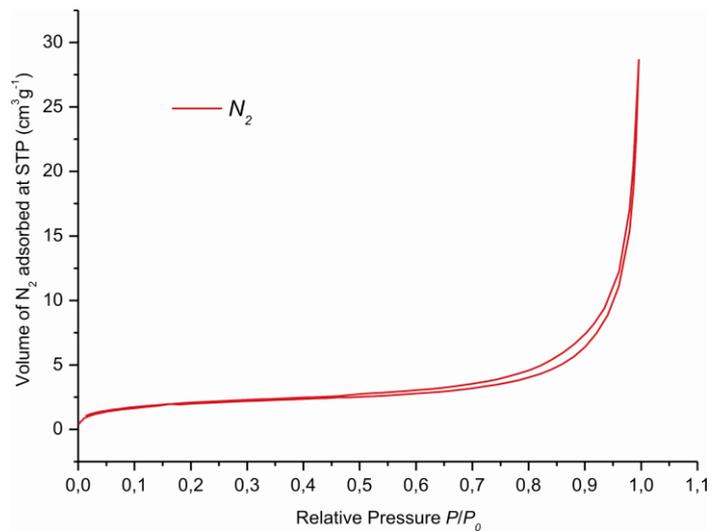


Figure S6. N_2 adsorption isotherm recorded on $\mathbf{1}_{act}$ at 77 K.

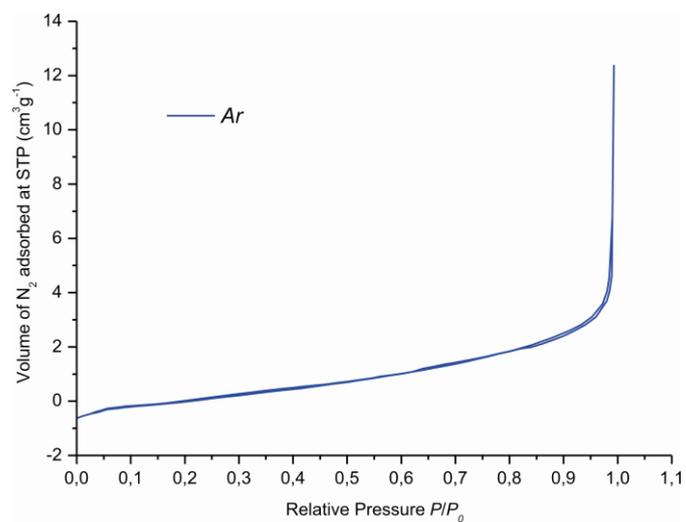


Figure S7. Ar adsorption isotherm recorded on $\mathbf{1}_{act}$ at 87 K.

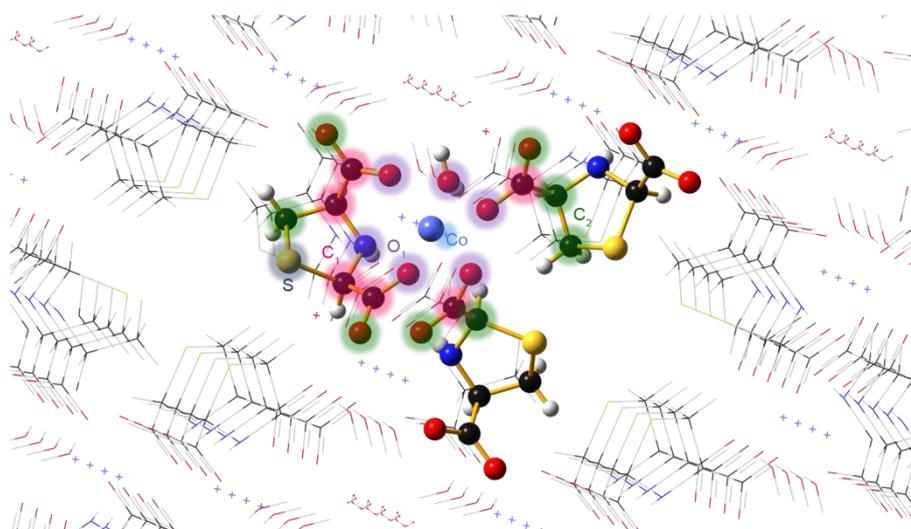


Figure S8. Structure of **1** obtained from the single crystal XRD refinement used as the starting point for the fitting procedure of the EXAFS data. Atoms included in the cluster used to compute phases and amplitudes are represented as spheres with the following color code: Co light blue, C black, O red, H white, N blue, S yellow. The three different shells of low Z atoms and the high Z Co and S atoms contributing to EXAFS signal are highlighted by different colored halos.

Table S1. Crystal data and structure refinement for **1**.

CCDC	855629	
Empirical formula	C ₅ H ₉ Co N O ₆ S	
Formula weight	270.13	
Temperature	100(2) K	
Wavelength	0.71069 Å	
Crystal system	Tetragonal	
Space group	<i>P</i> 4 ₁	
Unit cell dimensions	<i>a</i> = 12.335(4) Å	α = 90.°.
	<i>b</i> = 12.335(4) Å	β = 90.°.
	<i>c</i> = 5.265(3) Å	γ = 90.°.
Volume	801.1(9) Å ³	
Z	4	
Density (calculated)	2.165 Mg/m ³	
Absorption coefficient	2.398 mm ⁻¹	
F(000)	528	
Crystal size	0.05 x 0.05 x 0.1 mm ³	
Theta range for data collection	4.21 to 28.95°.	
Index ranges	– 15 ≤ <i>h</i> ≤ 16, – 15 ≤ <i>k</i> ≤ 16, – 7 ≤ <i>l</i> ≤ 7	
Reflections collected	4373	
Independent reflections	1769 [R(int) = 0.0325]	
Completeness to theta = 28.95°	87.4 %	
Refinement method	Full-matrix least-squares on F ²	
Data / restraints / parameters	1769 / 3 / 131	
Goodness-of-fit on F ²	0.996	
Final R indices [I > 2σ(I)]	R1 = 0.0280, wR2 = 0.0610	
R indices (all data)	R1 = 0.0333, wR2 = 0.0627	
Absolute structure parameter	– 0.010(17)	
Largest diff. peak and hole	0.551 and – 0.421 e.Å ⁻³	

Table S2. Atomic coordinates ($\times 10^4$) and equivalent isotropic displacement parameters ($\text{\AA}^2 \times 10^3$) for **1**. $U(\text{eq})$ is defined as one third of the trace of the orthogonalized U^{ij} tensor.

	x	y	z	$U(\text{eq})$
C(1)	2954(2)	-2057(2)	7195(6)	10(1)
C(2)	3448(3)	-3186(2)	7393(6)	13(1)
C(3)	4756(3)	-1694(2)	9008(6)	10(1)
C(4)	5016(3)	1048(3)	6402(6)	11(1)
C(5)	1866(2)	2062(2)	11684(6)	9(1)
N(1)	3837(2)	-1259(2)	7506(5)	10(1)
O(1)	4168(2)	1287(2)	7570(4)	13(1)
O(2)	4315(2)	-332(2)	12112(4)	11(1)
O(3)	2078(2)	-1009(2)	10465(4)	14(1)
O(4)	2081(2)	518(2)	6625(5)	19(1)
O(5)	2569(2)	1323(2)	11920(5)	12(1)
O(6)	26(7)	-137(6)	9637(17)	58(2)
S(1)	4397(1)	-3077(1)	9999(2)	13(1)
Co(1)	3212(1)	155(1)	9414(1)	9(1)

Table S3. (Selected) bond lengths [\AA] and angles [$^\circ$] for **1**. Refer to Figure 1(a) for the atom numbering.

C(1)-N(1)	1.477(4)
C(1)-C(2)	1.523(4)
C(1)-C(5)#1	1.537(4)
C(2)-S(1)	1.809(3)
C(3)-N(1)	1.483(4)
C(3)-S(1)	1.839(3)
C(4)-O(1)	1.250(4)
C(5)-O(5)	1.264(4)
N(1)-Co(1)	2.154(3)
N(1)-H(1)	0.80(4)
O(1)-Co(1)	2.069(2)
O(2)-Co(1)	2.056(2)
O(3)-Co(1)	2.080(2)
O(4)-Co(1)	2.075(3)
O(4)-H(4A)	0.840(19)

O(4)-H(4B)	0.812(19)
O(5)-Co(1)	2.109(2)
N(1)-C(1)-C(2)	107.9(2)
C(1)-C(2)-S(1)	104.0(2)
N(1)-C(3)-S(1)	107.6(2)
C(1)-N(1)-C(3)	112.4(2)
C(1)-N(1)-Co(1)	109.11(19)
C(3)-N(1)-Co(1)	108.53(19)
C(4)-O(1)-Co(1)	123.3(2)
C(5)-O(5)-Co(1)	133.6(2)
C(2)-S(1)-C(3)	90.56(15)
O(2)-Co(1)-O(1)	98.32(9)
O(2)-Co(1)-O(4)	175.48(10)
O(1)-Co(1)-O(4)	84.56(10)
O(2)-Co(1)-O(3)	93.42(9)
O(1)-Co(1)-O(3)	166.89(9)
O(4)-Co(1)-O(3)	83.38(10)
O(2)-Co(1)-O(5)	90.93(10)
O(1)-Co(1)-O(5)	92.68(9)
O(4)-Co(1)-O(5)	92.42(11)
O(3)-Co(1)-O(5)	92.96(9)
O(2)-Co(1)-N(1)	81.32(11)
O(1)-Co(1)-N(1)	97.11(10)
O(4)-Co(1)-N(1)	94.90(11)
O(3)-Co(1)-N(1)	78.84(10)
O(5)-Co(1)-N(1)	168.29(10)

Symmetry transformations used to generate equivalent atoms:

#1 y,-x,z-1/4 #2 -x+1,-y,z+1/2 #3 -x+1,-y,z-1/2 #4 -y,x,z+1/4

Table S4. Anisotropic displacement parameters ($\text{\AA}^2 \times 10^3$) for **1**. The anisotropic displacement factor exponent takes the form: $-2\pi^2 [h^2 a^{*2} U^{11} + \dots + 2 h k a^* b^* U^{12}]$

	U ¹¹	U ²²	U ³³	U ²³	U ¹³	U ¹²
C(1)	9(2)	13(2)	9(2)	-2(1)	-1(1)	-4(1)
C(2)	12(2)	14(2)	13(2)	-3(1)	0(1)	-1(1)
C(3)	9(2)	11(2)	10(2)	2(1)	1(1)	1(1)

C(4)	11(2)	11(2)	10(2)	-2(1)	-2(1)	-4(1)
C(5)	10(2)	10(2)	7(2)	-1(1)	0(1)	1(1)
N(1)	9(1)	12(1)	9(1)	1(1)	2(1)	-2(1)
O(1)	10(1)	11(1)	18(1)	2(1)	5(1)	1(1)
O(2)	12(1)	11(1)	11(1)	-3(1)	-2(1)	0(1)
O(3)	14(1)	12(1)	17(1)	-2(1)	4(1)	-3(1)
O(4)	16(1)	29(1)	13(1)	11(1)	-3(1)	-3(1)
O(5)	15(1)	10(1)	11(1)	-1(1)	0(1)	4(1)
S(1)	14(1)	9(1)	16(1)	1(1)	-3(1)	0(1)
Co(1)	8(1)	9(1)	10(1)	0(1)	0(1)	0(1)

Table S5. Hydrogen bonds for **1** [\AA and $^\circ$].

D-H...A	d(D-H)	d(H...A)	d(D...A)	\angle (DHA)
N(1)-H(1)...O(2)#5	0.80(4)	2.32(4)	3.117(4)	173(4)
O(4)-H(4A)...O(6)#1	0.840(19)	2.01(2)	2.830(8)	164(4)
O(4)-H(4A)...O(6)#6	0.840(19)	2.09(3)	2.841(9)	149(4)
O(4)-H(4A)...O(6)	0.840(19)	2.44(3)	3.098(9)	135(4)
O(4)-H(4B)...O(5)#5	0.812(19)	1.924(19)	2.735(4)	178(4)
O(4)-H(4B)...O(3)#7	0.812(19)	2.51(3)	3.027(4)	122(3)

Symmetry transformations used to generate equivalent atoms:

#1 $y, -x, z-1/4$ #2 $-x+1, -y, z+1/2$ #3 $-x+1, -y, z-1/2$ #4 $-y, x, z+1/4$ #5 $x, y, z-1$ #6 $-x, -y, z-1/2$ #7 $-y, x, z-3/4$

References

- [S1] B. Di Credico, G. Reginato, L. Gonsalvi, M. Peruzzini and A. Rossin, *Tetrahedron*, 2011, **67**, 267-274.
[S2] G. Pescitelli, T. Kurtan, U. Florke and K. Krohn, *Chirality*, 2009, **21**, E181-E201.